

# Highly supersonic motions within the outer features of the $\eta$ Carinae nebulosity

J. Meaburn<sup>1</sup>, P. Boumis<sup>1</sup>, J.R. Walsh<sup>2</sup>, W. Steffen<sup>1</sup>, A.J. Holloway<sup>1</sup>,  
R.J.R Williams<sup>1</sup> and M. Bryce<sup>1</sup>

<sup>1</sup>*Department of Physics and Astronomy, University of Manchester, Oxford Road, Manchester M13 9PL, UK.*

<sup>2</sup>*Space Telescope Coordinating Facility, ESO, Karl-Schwarzschild-Strasse 2, D-85748 Garching bei München, Germany.*

Accepted ????. Received ???.

## ABSTRACT

Spatially resolved  $H\alpha$  and  $[\text{N II}]$  line profiles have been obtained over striking features in the outer regions of the  $\eta$  Carinae nebula. The highly irregular outer ‘shell’ of low ionization,  $[\text{N II}]$  bright, knots has been shown to exhibit radial velocities between  $-1200$  and  $+300$   $\text{km s}^{-1}$  with respect to the systemic radial velocity, over its perimeter. Furthermore, several knots have been found which appear to emit only in the  $H\alpha$  line with radial velocities up to  $-1450$   $\text{km s}^{-1}$ .

However, the most intriguing features are a narrow ‘spike’ that projects through this outer shell and a faint ‘arc’ of emission that extends well beyond it. The ‘spike’, which exhibits a change of radial velocity along its length, could be a narrow collimated jet with an outflow velocity of  $\geq 1000$   $\text{km s}^{-1}$ . In one interpretation the ‘arc’ is modelled by a conical outflow and mechanisms for generating  $[\text{N II}]$  emission from highly supersonic gas are also discussed.

**Key words:**  $\eta$  Carinae.

## 1 INTRODUCTION

The complex nebulosity surrounding  $\eta$  Carinae represents the remnants of ejecta from this Luminous Blue Variable star ( $10^{6.6} L_{\odot}$  – Davidson et al, 1986) during irregular outbursts over the last 300 yrs (Walborn & Liller 1977). Investigations of the kinematics, morphologies and ionization mechanisms of the distinct regions identified in the sketch in Fig. 1 that comprise this nebulosity have been reported in a series of papers (hereafter referred to as Papers 1 – 3 ie. Meaburn, Wolstencroft & Walsh (1987), Meaburn, Walsh & Wolstencroft (1993 a) and Meaburn et al (1993 b) respectively). There is the dusty bi-polar Homunculus expanding at  $\approx 650$   $\text{km s}^{-1}$  (Paper 2) surrounded by a shocked, nitrogen enriched inner shell (identified by Walborn et al, 1978 as S ridge and W arc) with receding, expansive motions of  $\approx 350$   $\text{km s}^{-1}$  (Paper 1 and see Dufour, 1989). A knotty ‘jet’ projects through the NE quadrant of this inner shell (Hester et al 1991) whose episodic, outflow velocity is  $\leq 1500$   $\text{km s}^{-1}$  (Paper 3).

Outside these inner regions a variety of distinctly different phenomena are clearly apparent on UK Schmidt plates, Anglo-Australian Telescope (AAT) prime focus plates and the most recent HST images (Fig. 2 and see Sect. 2). There is the irregular, off-set outer ‘shell’ of knots partially identified by Walborn et al (1978). A feature now marked ‘spike’

in Fig. 1 (prematurely identified as a jet in Paper 1 – also see fig. 1(c) in Paper 2) projects through this irregular outer ‘shell’. This can be seen in the HST image in Fig. 2 to be  $\approx 0.3''$  wide. Also a potentially interesting feature of the outer nebulosity is the faint arc of nebulosity, marked ‘arc’ in Fig. 1 and outlined by a dashed line. This can be seen on a deep AAT prime focus plate to extend well beyond the perimeter of the outer shell in the vicinity of the ‘spike’ and to originate apparently in the vicinity of knot E5 (Walborn et al 1978).

The investigation of the dramatic kinematics of i) some of the prominent knots of the outer ‘shell’, ii) the ‘spike’ (already indicated in Paper 1) and iii) the ‘arc’ is reported in the present work. Spatially resolved profiles of the  $H\alpha$  and  $[\text{N II}]\lambda 6548$  and  $6584$  Å lines have now been obtained over these regions with the EMMI spectrometer on the ESO New Technology Telescope (NTT) in Chile.

Incidentally, a distance to  $\eta$  Carinae of 2.6 kpc will be adopted here to be consistent with Papers 2 & 3. This value is within the error bars of both the measurement of 2.5 kpc by Tapia et al (1988) for the distance to the adjacent OB stellar associations and the measurement of  $2.4 \pm 0.7$  kpc in Paper 2 based on the expansion velocity and proper motion of the Homunculus.

## 2 OBSERVATIONS AND RESULTS

Longslit spectral observations were obtained on the nights of the 10 & 11 March, 1993 using the echelle grating of the EMMI spectrometer on the NTT but from the remote observing facility at ESO Headquarters in Garching. The  $H\alpha$  and  $[N\ II]\lambda\ 6548\ \&\ 6584\ \text{\AA}$  emission lines were isolated by a  $90\ \text{\AA}$  bandwidth interference filter and the reciprocal dispersion was  $\approx 5\ \text{\AA}\ \text{mm}^{-1}$ . Cross dispersion was not employed. Partially resolved line profiles were obtained from the five slit positions marked 1 – 5 against a sketch of the outer features of  $\eta$  Carinae in Fig. 1. Many of these features can be seen in the HST image in Fig. 2, which was obtained with WFPC2 through filter F658N with an exposure of 400s (two frames coadded). In this display the inner features of the  $\eta$  Carinae nebula, that are sketched in Fig. 1, are burnt out. The raw data for this HST image was obtained from the Hubble Data Archive and processed using the 1995 set of WFPC2 parameters using WFPC2 pipeline in STSDAS (the images were obtained in Programme Numbers 5188 and 5239 with W. Sparks and Westphal as the principal investigators respectively).

A Loral CCD, with  $2048 \times 2048$ ,  $15 \times 15\ \mu\text{m}^2$  pixels, was used as the detector for the spectral observations. With this large detector the  $H\alpha$  and  $[N\ II]\lambda\ 6548\ \&\ 6584\ \text{\AA}$  lines were detected wholly in the 87th order of the  $31.6\ \text{grooves}\ \text{mm}^{-1}$  echelle grating and partially in both the 86th and 88th orders at much lower efficiency. However, the inclusion of the 86th and 88th orders permitted the unambiguous determination of the radial velocities of particularly high-speed flows. Spatially resolved line profiles were detected in 991 increments, each  $\equiv 0.364''$ , in the spatial dimension along each slit position and 1100 channels in the wavelength dimension. The slit width corresponded to  $1.2''$  on the sky ( $\equiv 10\ \text{km}\ \text{s}^{-1}$ ). The spectra were calibrated in wavelength to  $\pm 1\ \text{km}\ \text{s}^{-1}$  accuracy using the spectra from a Th/Ar emission line lamp. The spectrum of a tungsten lamp was used to both flat-field the data and correct for the blaze of the grating. The integration times were 1200 sec. The data were processed in the usual way using the FIGARO reduction software at the Manchester STARLINK node. The ‘seeing’ was  $\leq 1''$  throughout these latest spectral observations.

A first glance at the position-velocity (pv) arrays of profiles for Slits 1 – 5 suggested that the radial velocities of many of the knots of the outer shell were ambiguous simply because their extents in radial velocity are near to or greater than the separations of the  $H\alpha$  and two  $[N\ II]$  lines in the spectra. However, as the majority of the high-speed phenomena are brightest in the  $[N\ II]$  lines these ambiguities have been resolved. For example, a feature with a high approaching radial velocity appears shortwards of both the  $6548\ \text{\AA}$  and  $6584\ \text{\AA}$   $[N\ II]$  lines by the same amount and the strengths of the  $[N\ II]$  lines remain in fixed ratio.

The negative greyscale representations of the pv arrays of the line profiles along Slits 1-5 are shown in Figs. 3(a)-(e) respectively. These contain all the profiles of the  $H\alpha$  and the two  $[N\ II]$  lines in the 87th. order as well as high positive radial velocities in either the 86th. order (to the left of the display) or high negative radial velocities in the 88th order (to the right).

The spatial extents of these displays correspond to the lengths of the slits marked in Figs. 1 & 2. The various veloc-

ity features, which are numbered in the spectra, are identified along the five slit lengths over enlargements of the image in Fig. 2 in Figs. 4(a)-(b). The values of  $V_{\text{HEL}}$  of the peak of the  $[N\ II]\lambda\ 6584\ \text{\AA}$  brightnesses for the knots identified in Figs. 4(a)-(b) are listed in Table 1 along with estimates ( $\pm 10$  percent) of the corresponding  $[N\ II]\lambda\ 6584\ \text{\AA} / H\alpha$  brightness ratios (again at the peak brightnesses for the features have nearly the same extent in both lines), where these ratios are unconfused.

The measurement of  $V_{\text{HEL}}$  for a minority of the knots in this way is not possible for these are characterised by only a single feature in the pv arrays in Figs 3(b), (c) & (d). If these features are considered real and not instrumental artefacts one interpretation is that they are produced by knots with extreme radial velocities where the  $H\alpha$  line is dominant. The knots in question are starred in Table 1. In all cases these appear to be real features in the pv arrays for they also are present in the 88th order to the right hand side of each display.

The feature that poses the greatest problem in this respect is the looped structure in Fig. 3(d) sub-divided somewhat arbitrarily as separate Slit 4 Knots 1-3. Certainly Knot 3 appears in all three lines with  $V_{\text{HEL}} \approx -200\ \text{km}\ \text{s}^{-1}$  but the interpretation of the components identified as Knots 1 & 2 in Fig. 3(d) as part of a coherent feature in the pv array of  $[N\ II]\lambda\ 6548\ \text{\AA}$  profiles, though superficially persuasive, must remain doubtful. If these two knots have their origin in the  $[N\ II]\lambda\ 6548\ \text{\AA}$  profiles then they should be clearly present in the three times brighter  $[N\ II]\lambda\ 6584\ \text{\AA}$  profiles. Tests on the data have demonstrated their absence in the  $[N\ II]\lambda\ 6584\ \text{\AA}$  profiles at the appropriate level. This raises the possibility that Knots 1 & 2 are exclusively bright in the  $H\alpha$  line but with very high negative radial velocities (starred for Slit 4 in Table 1). Within this (uncertain) interpretation it is then only a chance overlap that creates the impression of a coherent velocity feature for Knots 1-3 in Fig. 3(d). However, such a chance alignment for such very different ranges in radial velocity seems highly unlikely. Consequently, in Sect. 3.3, a dual interpretation of this strange velocity feature that comprises Slit 4 Knots 1-3 will be presented.

## 3 DISCUSSION

New kinematical information has been obtained for three separate features of the  $\eta$  Carinae nebula. The implications for the ‘outer shell’ of knots, the ‘spike’ and the ‘arc’ will now be discussed along with consideration of the mechanisms that cause the ionization of the high-speed ejecta.

### 3.1 The ‘polar blowout’ model

If the knots in the outer ‘shell’ in Figs. 1 & 2 form part of a coherent feature then it is firstly notable that its centroid is offset by  $\approx 12''$  to the NE of  $\eta$  Carinae. In any case a simple interpretation of this whole feature as a radially expanding irregular shell is apparently contradicted by the kinematical observations shown in Figs. 3(a)-(c). This contradiction is epitomised by the profiles in the pv array along Slits 1, 2 & 3 in Figs. 3(a),(b) & (c) respectively, which pass over what

Slit N <sup>o</sup> .	Knot N <sup>o</sup> .	$V_{\text{HEL}}$ ( $\text{km s}^{-1}$ )	Ratio
1	1	-200	2.4
	2	-50	-
	3	-100	-
	4	+450	3.0
	5	+250	3.5
2	1(a-c)	-300, -200, -100	-
	2(a,b)	-250, -300	3.8
	2(c,d)	-150, -50	3.8
	3(a,b)	-900, -800	-
	4 ('spike')	-650	2.9
	5	-1200	2.0
	6	-950	1.8
	7	+250	-
	8	-550	2.5
	9	+300	-
10*	-1250*	-	
3	1	-250	3.5
	2 (E5)	-140	3.5
	3	-200	3.5
	4	+250	-
	5 ('spike')	-850	2.2
	6*	-1450*	-
4	1* ('arc')	-1400* or -730	-
	2* ('arc')	-1300* or -630	-
	3 ('arc')	-250	-
	4	+300	-
5	1	-400	-

**Table 1.** Motions of the outer shell. (\*) These knots are single features in the pv arrays. The starred radial velocities assume that they are of  $\text{H}\alpha$  origin and alternative unstarred values (for Slit 4 Knots 1 & 2) if of  $[\text{N II}]\lambda 6548\text{\AA}$  origin. The peak intensity ratio of  $[\text{N II}]\lambda 6584\text{\AA} / \text{H}\alpha$  is given in the final column. Also note that the systemic radial velocity for  $\eta$  Carinae is  $V_{\text{HEL}} = -7\text{km s}^{-1}$

(Paper 2).

could be the edge of the outer ‘shell’. In these arrays, certainly detected velocity features, which are bright in the  $[\text{N II}]$  lines, extend all the way out to  $\approx -1200\text{ km s}^{-1}$  (eg. see Slit 2 Knot 5) from the systemic radial velocity. Single profiles at the systemic radial velocity ( $V_{\text{HEL}} \approx -10\text{ km s}^{-1}$ ) would be expected to characterise the edge of a simple, radially expanding shell. Even more extreme  $\text{H}\alpha$  bright knots are suggested out to  $-1450\text{ km s}^{-1}$  (eg. see Slit 3 Knot 6 and Slit 2 Knot 10).

The complex profiles in the pv array in Fig. 3(a) from the knots along the north eastern edge of the outer shell, covered by Slit 1, exhibit approaching, radial velocities out to  $\approx -200\text{ km s}^{-1}$  from an extended region, as well as a component at the systemic radial velocity. However, the knots in the north western quadrant of the outer ‘shell’, covered also by Slit 1, emit the  $[\text{N II}]$  line from a region  $1''$  across whose profiles have FWHMs of  $\approx 80\text{ km s}^{-1}$  but are displaced to *receding* radial velocities of  $\approx +250\text{ km s}^{-1}$  with respect to the systemic radial velocity. Note that the nearby ‘lobe’ of the inner shell (identified in Fig. 1) and the southern part of this shell (S Ridge in Walborn et al 1978) was shown in Paper 1 to emit red-shifted line profiles out to  $+400\text{ km s}^{-1}$  with respect to the systemic radial velocity (see Slits 12''N

and 4, 8 & 12''S in fig. 5 of Paper 1). Some of the present (and previous - see Papers 1, 2 & 3) kinematical observations are then consistent with the ‘polar blowout’ model of Hester et al (1991) (and its precursor model in Paper 1 - see fig. 8(b)). What is loosely described as the outer ‘shell’ of knots in Fig. 1 is composed nearly exclusively of ionized material flowing towards the observer even around its perimeter. These knots (and the ‘jet’ - see Paper 3) must all then be a consequence of an approaching outflow on the nearside of the bi-polar axis of the dusty Homunculus reflection nebula (Paper 2). The SE lobe of the Homunculus is approaching and the NW receding from the observer along a common axis tilted at  $33^\circ$  to the plane of the sky. Within the ‘polar blowout’ model the ‘inner shell’ and ‘lobe’ in Fig. 1 are then on the far side of the Homunculus and flowing away from the observer.

The ‘spike’ and ‘arc’ in Fig. 1 are similarly flowing towards the observer but are elongated well beyond the SE end of the bi-polar axis of the Homunculus. They would clearly have to have an extreme configuration to make them part of a simple ‘polar blowout’ from the centre of the Homunculus but are likely to be closely related to this eruptive event.

### 3.2 The ‘spike’ as a jet

Of particular interest are the line profiles over the ‘spike’ intercepted by Slit 2 in Fig. 1. These are characterised in the pv array in Fig. 3(b) by a bright  $[\text{N II}]$  emission feature,  $\approx 1''$  across that has a FWHM of only  $60\text{ km s}^{-1}$  but displaced from the systemic radial velocity by  $\approx -650\text{ km s}^{-1}$  (Slit 2, Knot 4 in Table 1 and Fig. 3(b)). A faint velocity component can be traced in the same pv array from this approaching radial velocity right back to the systemic radial velocity. The ‘spike’ is also intercepted by Slit 3 (Knot 5 in Fig. 3(c) and Table 1) where it now has  $V_{\text{HEL}} \approx -850\text{ km s}^{-1}$ .

The present kinematical observations of the ‘spike’ along Slit 2 should be interpreted along with those from it but nearer to  $\eta$  Carinae in Paper 1 (EW slit positions  $8''$  &  $12''$  S - fig. 5 in that paper). The pv arrays across the ‘spike’ for these two previous positions reveal a spatially resolved velocity feature that extends continuously out to  $\approx -700\text{ km s}^{-1}$  from the systemic radial velocity.

The ‘spike’ identified in Fig. 1 and seen in Fig. 4(b) has a width of a few arcseconds within the ‘inner shell’ of collisionally ionized gas (see Paper 1) and decreases from  $\approx 0.35''$  at  $18''$  from  $\eta$  Carinae (where it is intercepted by Slit 2) to  $0.25''$  at  $26''$  (Slit 3). An elongated cavity, with thin outflowing walls was suggested as an explanation of this feature in Paper 1. It was proposed that the spike-like appearance arose as the cavity walls were viewed tangentially. The present kinematical observations (which are further from  $\eta$  Carinae than the earlier ones) and the HST imagery suggest that the ‘spike’ could be a jet ie. a narrow, collimated outflow exhibiting some form of acceleration or directional variation to produce a change of  $V_{\text{HEL}}$  from  $-650\text{ km s}^{-1}$  to  $-850\text{ km s}^{-1}$  between its interception by Slits 2 & 3.

An estimate of the outflow velocity of the ‘spike’, if a jet, depends critically on its orientation with respect to the plane of the sky. One guide to this angle,  $\alpha$ , could be the measured orientation for E5 (see Fig. 1). This has been derived from the proper motion of  $5''/\text{century}$  of E5 from  $\eta$  Carinae (Wal-

born & Blanco 1989) which, for a distance of 2.6 kpc combined with the radial velocity difference of  $\approx -140 \text{ km s}^{-1}$  (Table 1) gives an outflow velocity of  $620 \text{ km s}^{-1}$  tilted at  $\alpha = 13^\circ$  to the sky for this group of knots E5 marked in Fig. 1. With this same angle a speed of  $\approx 3800 \text{ km s}^{-1}$  is then predicted by the measured value of  $V_{\text{HEL}} = -850 \text{ km s}^{-1}$  for the tip of the ‘spike’. For a constant velocity away from  $\eta$  Carinae the ‘spike’ would then have originated in an eruptive event around 1890. This is near the time of major outbursts listed by Walborn & Liller (1977).

Perhaps, the orientation of the ‘spike’ can be estimated more realistically if it is assumed that its directional variations *in the plane of the sky*, which give an apparent change of  $15^\circ$  between where it is intercepted by Slits 2 and 3, are of similar magnitude to directional changes perpendicular to the plane of the sky. This would cause the radial velocity difference of  $-200 \text{ km s}^{-1}$  between these two positions even if, more realistically, no acceleration is assumed. In this case  $\alpha \approx 37^\circ$  is predicted with a jet speed of  $1077 \text{ km s}^{-1}$  giving an age of  $\approx 360 \text{ yr}$  for the tip of the ‘spike’, which is before records of the eruptions of  $\eta$  Carinae are available though this speed must be subject to large uncertainties.

Incidentally, the converging sides of the ‘spike’ can be explained as part of a jet structure if the  $[\text{N II}]$  emission is from recollimation shocks (cf. Paper 3). A model of the spectrum of Davidson et al. (1986) of an  $[\text{N II}]$  bright knot in the outer shell of the  $\eta$  Carinae nebula (by John Raymond and reported in Meaburn et al. (1988)) gave a shock velocity of  $140 \text{ km s}^{-1}$ . In any case, the shock velocities cannot be higher than this value for the small knots in the outer shell of  $\eta$  Carinae to be ionized by radiative shocks. Since  $[\text{N II}]$  emission requires the shocks to be  $\leq 100 \text{ km s}^{-1}$ , the aspect ratio of the convergent part of the spike will be roughly  $v_{\text{jet}}/(2 v_{\text{shock}})$ , i.e.  $\geq 5:1$  in projection for a jet speed of  $1077 \text{ km s}^{-1}$  which is easily satisfied by the observed high aspect ratio of the ‘spike’.

### 3.3 The ‘arc’ as a conical flow

Unusual kinematical features also occur along Slits 4 & 5 over the ridge marked ‘arc’ in Fig. 1 which appears to originate near the knot marked E5. Incidentally, a detailed inspection of the HST image in Fig. 2 reveals that both E5 and the northern end of the ‘arc’ are composed of a conglomeration of emission line knots as small as  $0.3''$  across. It is in the profiles from Slit 4 over this ‘arc’ that the strange loop (discussed in Sect. 2) in the pv arrays occurs (Slit 4 Knots 1 – 3 in Fig. 3(d) and Table 1). The kinematical features over E5 are themselves complex (Fig. 3(c)). A ‘parabola’ of emission in the pv array (Slit 3 extended Knot 2),  $15''$  across, extends out to  $-400 \text{ km s}^{-1}$  from the systemic radial velocity though the peak of the emission from E5 can be seen, in the contour map of the  $[\text{N II}]\lambda 6584\text{\AA}$  surface brightnesses shown in Fig. 6, to be at  $V_{\text{HEL}} \approx -140 \text{ km s}^{-1}$ .

Assuming the interpretation of the loop as a coherent feature of  $[\text{N II}]\lambda 6548\text{\AA}$  emission (though see the reservations expressed in Sect. 2) an attempt has been made to reproduce the approaching ‘loop’ in the pv array in Fig. 3(d) from the ‘arc’ sketched in Fig. 1 using the model shown in Fig. 7(c). Here a conical shell is assumed to have a ratio of thickness to radius of 0.15. The ionized gas within this shell is given, somewhat arbitrarily, a flow velocity along its

surface of  $1500 \text{ km s}^{-1}$  (similar to the well-verified speed of the jet in Paper 3). The full opening angle of the cone from the image in Fig. 2 and the AAT photograph is taken to be  $26^\circ$ . The angle between the axis of the cone and the plane of the sky is  $18^\circ$ . The slit is oriented at  $30^\circ$  with respect to the axis of the cone to simulate approximately its orientation to the ‘arc’ in Fig. 1. The predictions of this model (Fig. 7(b)) convincingly match the contour plot of the observed array of profiles in Fig. 7(a) (if these are all assumed to be of  $[\text{N II}]\lambda 6548\text{\AA}$  origin). Uniform volume emissivity of the line emission within the cone would give rise to a completely closed ellipse in the predicted pv array in Fig. 7(b). However, in the model, the volume emissivity has been reduced in one section of the cone until a reasonable match was achieved to the brightness variations within the observed loop in the pv array. This self consistent set of key parameters (the opening angle, the speed and the angle between the cone’s axis and the sky) is constrained to within ten percent by the radial velocity range of  $\sim -130$  to  $-900 \text{ km s}^{-1}$  respectively in the observed pv array from the ‘arc’ (Figs. 3(d) and 7(a)). An outflowing cone of line emitting knots, perhaps starting in an, as yet unspecified, manner from the brighter E5 group of knots, is therefore suggested as the explanation of this arc-like feature.

The absence of the comparable radial velocity components in the  $[\text{N II}]\lambda 6584\text{\AA}$  line profiles makes this interpretation of the ‘loop’ uncertain. However, one possible way of suppressing the comparable  $[\text{N II}]\lambda 6584\text{\AA}$  emission features (for Slit 4 Knots 1 & 2) with approaching radial velocities could be if a localised, but foreground, receding flow of  $\text{H II}$  gas was present with sufficient density to absorb only the most negative high velocity  $[\text{N II}]\lambda 6584\text{\AA}$  features. It may be relevant that there is a positive velocity extension in the  $\text{H}\alpha$  pv array over this for Slit 4 in Fig. 3 d. This mechanism however requires the electron temperature,  $T_e$ , high enough so that the foreground column of  $\text{H}(n=2)$  has  $\tau_{\text{H}\alpha} \gg 1$  but also  $T_e$  low enough that it is fainter than the  $[\text{N II}]$  itself and since  $\tau_{[\text{N II}]} \ll 1$  this may be difficult.

The alternative interpretation of Slit 4 Knots 1 & 2 as emitting  $\text{H}\alpha$  only would of course invalidate the model for the ‘arc’ in Fig. 7(c). Note that a measured decline in the  $[\text{N II}]\lambda 6584\text{\AA} / \text{H}\alpha$  ratio is shown in Fig. 5 which suggests that knots with extreme radial velocities (starred in Table 1) could be undetectable in both the  $[\text{N II}]\lambda 6548\text{\AA}$  and  $[\text{N II}]\lambda 6584\text{\AA}$  lines but still at  $\text{H}\alpha$ . Incidentally Raymond (1991) has demonstrated that pure Balmer line emission can be produced by non-radiative shocks in partially neutral gas. A decisive test of these two alternative interpretations of this loop in the pv array shown in Fig. 3(d) awaits observations of the  $[\text{S II}]\lambda 6716$  &  $6731\text{\AA}$  lines. The looped velocity feature could be detected unambiguously in such observations.

### 3.4 Ionization mechanisms

Similar to E5 (Sect. 3.3), all of the major groups of low ionization knots that constitute the ‘outer shell’ in Fig. 1 have measurable proper motions away from  $\eta$  Carinae (Walborn & Blanco 1989). These large proper motions alone favour their origin in bullets of plasma ejected from  $\eta$  Carinae (during the outburst 150 years ago) but now ploughing into slower moving material perhaps from previous ejections. In this case, a fundamental problem is immediately encoun-

tered. If the velocities of the bullets relative to the ambient gas are  $\geq 1000 \text{ km s}^{-1}$ , as suggested for many of the supersonic features revealed in Figs. 3(a)-(e), then bow-shock velocities of the same magnitude are anticipated which should generate post-shock emission at X-ray wavelengths at their apices (which are observed from both the ‘lobe’ and the region of the ‘spike’ and E5 in Fig. 1 by Chlebowski et al (1984)). Shock velocities must be restricted to  $\leq 100 \text{ km s}^{-1}$  for the post-shock emission of [N II] nebular lines that are observed here (e.g. Raymond 1979), which would only occur for material passing very obliquely through the extreme wings of any bow-shocks around such high-speed bullets.

A similar difficulty was encountered in interpreting [N II] line profiles along the ‘jet’ in Paper 3 for it is flowing, episodically, at a speed of  $\leq 1500 \text{ km s}^{-1}$  away from  $\eta$  Carinae. It was suggested that the narrow, highly blue-shifted [N II] profiles from the knots in the ‘jet’ originate in slow shocks driven into dense bullets rather than from the post bow-shock regions around the bullets.

Emission of the highly blue-shifted [N II] profiles from behind a bow-shock around a high-speed bullet encountering an  $\approx 100 \text{ km s}^{-1}$  slower shell could also be considered to overcome this problem. This mechanism could explain the knots which exhibit a very narrow range of radial velocities, albeit highly shifted from the systemic, eg. that are seen in the western part of the pv array in Fig. 3(a). However, the large range in radial velocities of some of the phenomena reported here (eg. over the ‘spike’ and ‘arc’ in Fig. 1) are not compatible with post bow-shock emission from bullets and ambient gas which have small differential velocities.

The fine-scale knottiness of all the emission regions seen in Figs. 2, 4(a) and (b) may suggest that the ejecta fragments take the form of ‘grape-shot’ rather than individual ‘bullets’. Cid-Fernandes et al (1996) have recently shown how individual clumps in the ejecta of supernovae can be fragmented into ‘grape-shot’ as they pass through a reverse shock. These grape-shot clumps then propagate easily through the shocked ejecta and shocked ambient medium before colliding directly with the external ambient medium, at velocities little less than those at which they were driven by the initial explosion. Similar processes may well occur in outburst ejecta such as those seen in  $\eta$  Car.

If the individual globules within the cloud of condensations are at least 150 times as dense as the surrounding medium, the reverse shocks driven into  $1200 \text{ km s}^{-1}$  ejecta will be slow enough to radiate [N II] at velocities close to the ejecta velocity (cf. Slit 2 Knot 5; in contrast  $1500 \text{ km s}^{-1}$  ejecta such as Knot 10 may still be non-radiative, or at least have fast enough reverse shocks to prevent [N II] emission). Once the reverse shocks have traversed the clumps, they will be rapidly dispersed by turbulence eddies, and mixed with gas from the ambient medium. The residual momentum of this lower density gas will drive weak shocks into the surrounding ambient medium. Succeeding blobs will encounter this mildly-shocked ambient medium, which would now have a  $100 \text{ km s}^{-1}$  or so outward velocity and an increased gas density. Before they overtook the shock driven by the first generation of blobs, doubly-shocked ambient gas would generate [N II] emission at velocities up to  $200 \text{ km s}^{-1}$ . In particular, this may be the explanation for structures such as Slit 2 Knots 2(a-d).

While Cid-Fernandes et al (1996) have provided initial

theoretical support for the possibility of such mechanisms, much work beyond the scope of the present paper is required to fully model the origin and evolution of grape-shot ejecta.

## 4 CONCLUSIONS

1) The ‘outer shell’ of low ionization knots is not expanding radially for knots can be found with a large range of radial velocities on its perimeter ( $V_{\text{HEL}} = -1200 \text{ km s}^{-1}$  to  $+300 \text{ km s}^{-1}$ ). Even some knots, emitting  $\text{H}\alpha$  only, may have  $V_{\text{HEL}} = -1450 \text{ km s}^{-1}$ . Some association with a ‘polar blowout’ is favoured.

2) Changes in both radial velocity and direction of the ‘spike’ favour its interpretation as a continuous ‘jet’ with a speed of  $1080 \text{ km s}^{-1}$ .

3) The observations of the ‘arc’ remain ambiguous. A coherent loop in the pv array of [N II] $\lambda$  6548Å profile suggests that it could be a narrow cone with an outflow speed of  $1500 \text{ km s}^{-1}$ . The absence of the most negative velocity features in the corresponding [N II] $\lambda$  6584Å profiles casts doubt on this interpretation. Somewhat artificial means can be introduced to overcome this problem. Alternatively, the loop is composed of  $\text{H}\alpha$  profiles at extreme negative radial velocities and [N II] $\lambda$  6548Å profiles at more modest radial velocities. In this case a most fortuitous alignment of velocity components must occur to give the coherent appearance of the loop. Observations of [S II] profiles are needed to resolve the issue.

4) A ‘grape-shot’ model is proposed to explain the knottiness of much of the emission seen in HST images.

## 5 ACKNOWLEDGEMENTS

We wish to thank the staff at the New Technology Telescope, La Silla, and the remote observing facility, Garching for their excellent assistance during these observations.

WS and RJRW are grateful to PPARC for receipt of the Post Doctoral Research Associateships, AJH a Post Graduate Research Studentship and MB a University of Manchester Research Fellowship.

## 6 LEGENDS

### Figure 1

The five slit positions, 1-5 are shown against a sketch of the principal features of the  $\eta$  Carinae nebulosity. The spatial extents of the position-velocity (pv) arrays shown in Figs. 3(a)-(e) are indicated by the lengths of the lines which mark the slit positions.

### Figure 2

A deep negative print of the HST image of the  $\eta$  Carinae nebulosity, in the light of [N II] $\lambda$  6584Å, in which the features of the outer shell are revealed.

### Figure 3

Negative greyscale representations (whose total extents are marked in Figs. 1 & 2) of the pv arrays of  $\text{H}\alpha$  and [N II] profiles are shown for Slits 1-5 in (a) – (e) respectively. The

87th. order of the echelle spectrum, containing all three lines is in the centre of the display. Part of the 86th. order is to the left and part of the 88th order to the right. The dark vertical bands are from the background nebular emission in these three lines. Dark horizontal bands are continuous spectra of star images which have also fallen on the slit.

Each separate velocity feature in these displays is identified by a number which is also marked against the nebular image in Figs. 4(a) & (b). and listed in Table 1.

#### Figure 4

(a) Slit 1 is shown against an enlargement of the image in Fig. 2. The positions and extents of the velocity features identified in Figs. 3(a)-(e) are shown. Each is tentatively called a Knot in Table 1. (b). As for (a) but for Slits 2-5.

#### Figure 5

The  $[\text{N II}]\lambda 6584\text{\AA}$  /  $\text{H}\alpha$  brightness ratios v.  $V_{\text{HEL}}$  for the knots on Table 1. All values are for the peaks of the surface brightnesses of the velocity features in the pv arrays.

#### Figure 6

A contour map of the surface brightnesses of the pv array of  $[\text{N II}]\lambda 6584\text{\AA}$  profiles for Knot 2 along Slit 3 (E5 in Fig. 1). The intervals are linear.

#### Figure 7

(a) A contour map, with linear intervals, of the pv array of  $[\text{N II}]$  line profiles for slit Pos. 4 which is shown in Fig. 3(d). The two scales in radial velocity reflect the uncertain interpretation (as either of  $[\text{N II}]\lambda 6548\text{\AA}$  or  $\text{H}\alpha$  origin) of Knots 1 & 2. The ‘loop’ to negative radial velocities is from the ‘arc’ marked in Fig. 1. (b) The predicted pv array from the model in (c) which closely matches the observations within the  $[\text{N II}]\lambda 6548\text{\AA}$  interpretation of Knots 1 & 2 in (a). (c) The ‘arc’ in Fig. 1 modelled as a conical outflow at  $1500 \text{ km s}^{-1}$  again within the  $[\text{N II}]\lambda 6548\text{\AA}$  interpretation. The slit (the vertical rectangle) is at an angle to the axis of this cone to approximately match its position for the observations.

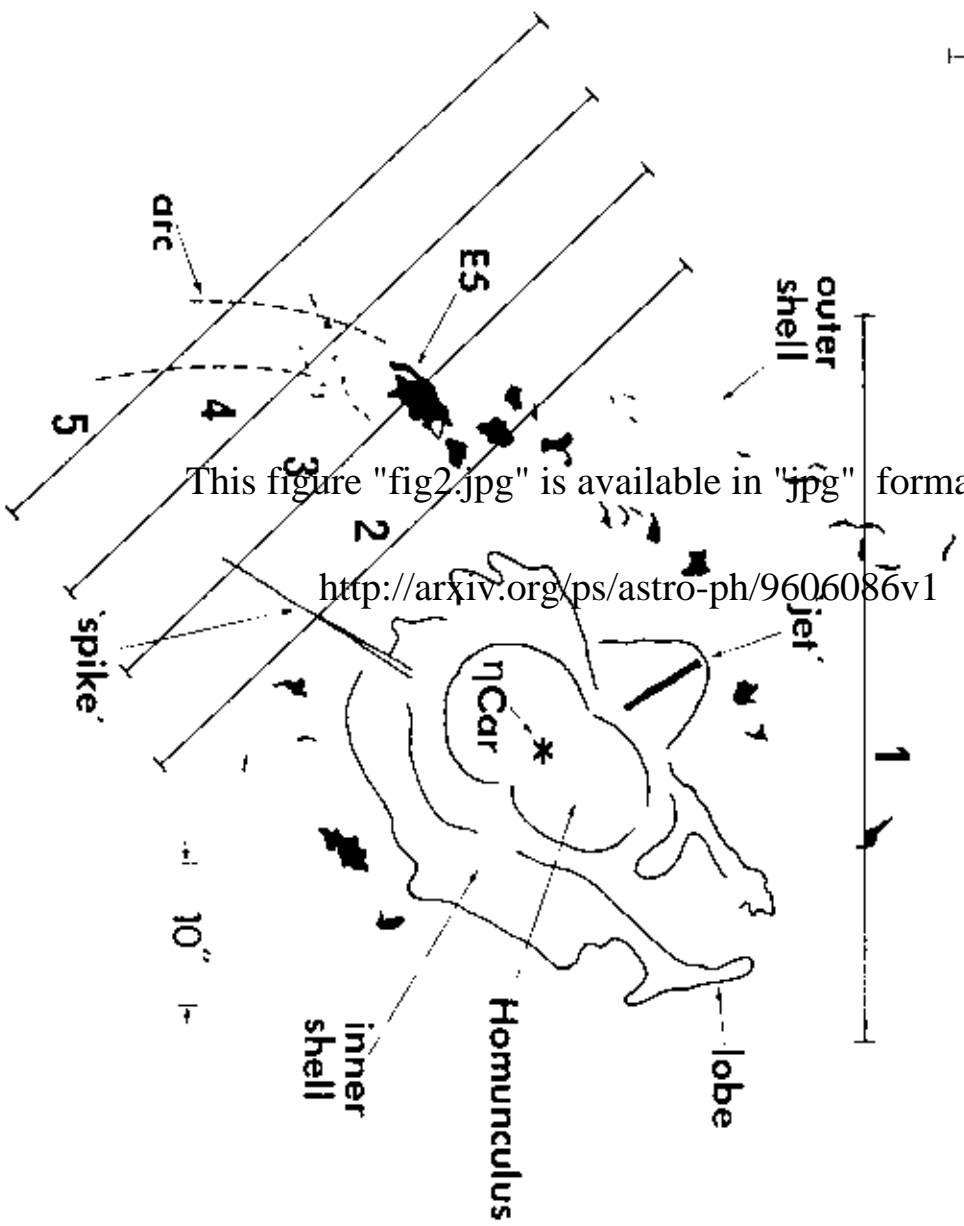
## REFERENCES

- Chlebowski, T., Seward, F.D., Swank, J. & Szymkowiak, A., 1984, *ApJ*, 281, 665.  
 Cid-Fernandes R., Plewa T., Różycka M., Terlevich R., Tenorio-Tagle G., Franco J., Miller W., 1996, *MNRAS*, in press  
 Davidson K., Dufour R.J., Walborn N.R. & Gull T.R., 1986, *ApJ*, 305, 867.  
 Dufour R.J., 1989, *Rev.Mex.A.A.*, 18, 87.  
 Hester J.J., Light R.M., Wetsphal J.A., Currie D.G., Groth E.J., Holtzman J.A., Lauer T.R., O’Neil E.J., 1991, *AJ*, 102, 654.  
 Meaburn J., Wolstencroft R.D. & Walsh J.R., 1987, *A&A*, 181, 333. (Paper 1)  
 Meaburn J., Wolstencroft R.D., Raymond J.C., Walsh J.R. & Lopez J.A., 1988, in ‘Dust in the Universe’, eds. Bailey, M.E. & Williams, D.A., Cambridge University Press, 381.  
 Meaburn J., Walsh J.R. & Wolstencroft R.D., 1993a, *A&A*, 268, 283. (Paper 2)

- Meaburn J., Gehring G., Walsh J.R., Palmer J.W., Lopez J.A., Bryce M. & Raga A.C., 1993b, *A&A*, 276, L21. (Paper 3)  
 Raymond J.C., 1979, *ApJ*, 39, 1.  
 Raymond J.C., 1991, *PASP*, 103, 781.  
 Tapia M., Roth M., Marraco H. & Ruis M.T., 1988, *MNRAS*, 232, 661.  
 Walborn N.R. & Liller M.H., 1977, *ApJ*, 211, 181.  
 Walborn N.R., Blanco B.M., Thackeray A.D., 1978, *ApJ*, 219, 498.  
 Walborn N.R., Blanco B.M., 1988, *PASP*, 100, 797.

This paper has been produced using the Royal Astronomical Society/Blackwell Science  $\text{\LaTeX}$  style file.

Fig. 1



This figure "fig2.jpg" is available in "jpg" format from:  
<http://arxiv.org/ps/astro-ph/9606086v1>

This figure "fig3a.jpg" is available in "jpg" format from:

<http://arxiv.org/ps/astro-ph/9606086v1>

This figure "fig3b.jpg" is available in "jpg" format from:

<http://arxiv.org/ps/astro-ph/9606086v1>

This figure "fig3c.jpg" is available in "jpg" format from:

<http://arxiv.org/ps/astro-ph/9606086v1>

This figure "fig3d.jpg" is available in "jpg" format from:

<http://arxiv.org/ps/astro-ph/9606086v1>

This figure "fig3e.jpg" is available in "jpg" format from:

<http://arxiv.org/ps/astro-ph/9606086v1>

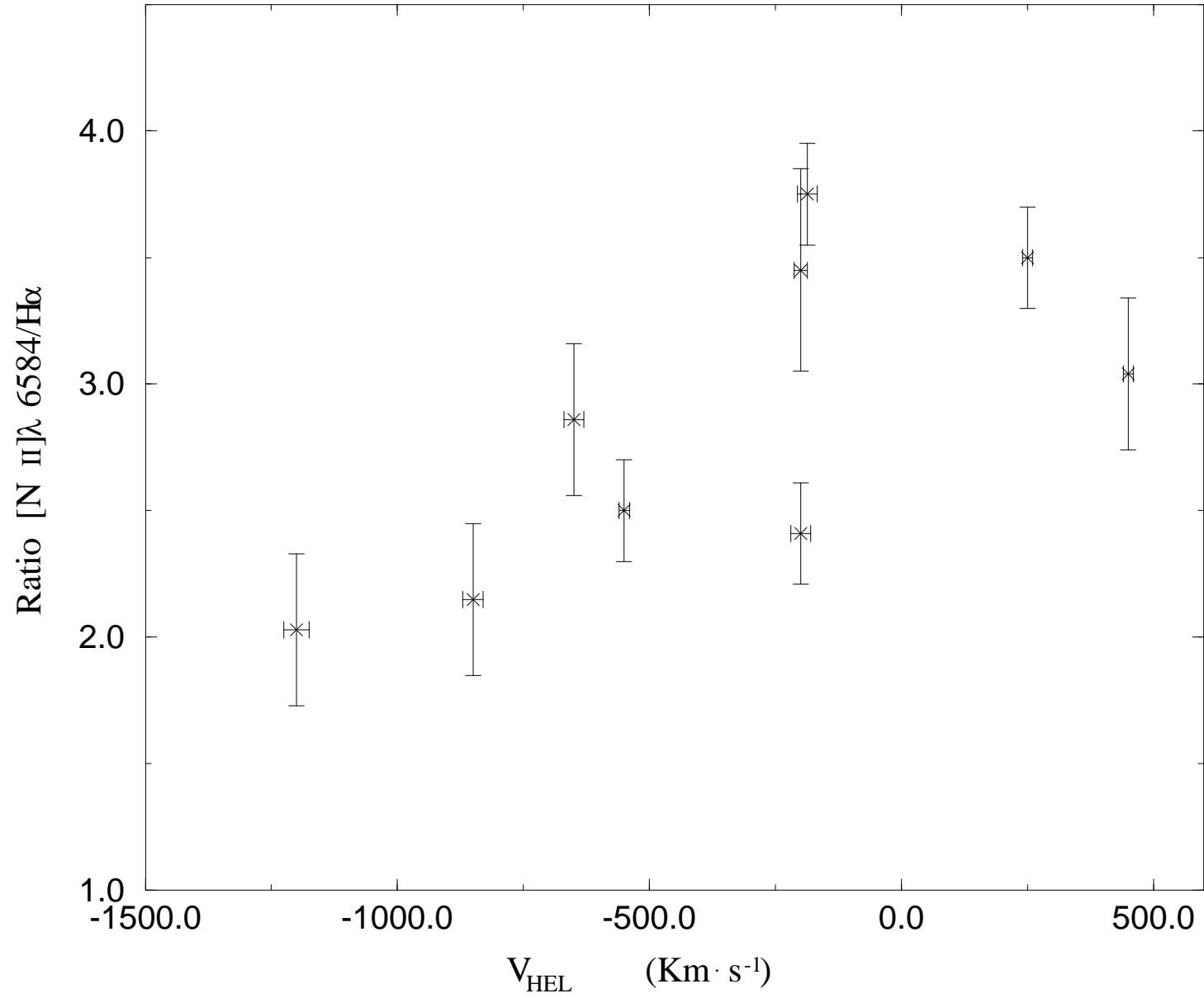
This figure "fig4a.jpg" is available in "jpg" format from:

<http://arxiv.org/ps/astro-ph/9606086v1>

This figure "fig4b.jpg" is available in "jpg" format from:

<http://arxiv.org/ps/astro-ph/9606086v1>

# Eta Knots



SLIT 3

[N II] $\lambda$  6584 Å

